Nanoscale



PAPER

View Article Online
View Journal



Cite this: DOI: 10.1039/d5nr05056a

# Artificial synaptic behaviors of a mobile silver-doped vanadium–cerium oxide memristor with embedded silver nanoclusters for neuromorphic computing applications

Jiyeon Ryu,[a] Peter Hayoung Chung,[a] Cheolhwan Yoon,[b] Minkook Kang,[a] Hyung-Joon Shin *[b,c] and Tae-Sik Yoon *[a,b]

Although mobile metal-ion-based filamentary memristors are explored as an artificial synapse for neuromorphic computing, they suffer from abrupt and stochastic switching. Hence, this study reports a non-filamentary synaptic memristor using mobile silver-doped vanadium–cerium oxide ($VCeO_x$:Ag) that achieves linear and symmetric conductance modulation with stable endurance over $10^4$ potentiation/depression cycles through a conduction combined with Ag nanoclusters and redistributed mobile Ag ions. This conjugated contribution enables polarity-dependent, robust and reproducible analog switching. Transmission electron microscopy (TEM) analysis confirms the presence of Ag nanoclusters, and Kelvin probe force microscopy (KPFM) verifies the field-driven migration and redistribution of residual Ag ions. Time-dependent synaptic plasticity properties, including paired-pulse facilitation (PPF), post-tetanic potentiation (PTP), spike-rate-dependent plasticity (SRDP) and short-term-to-long-term memory (STM-to-LTM) transitions, are harnessed to implement reservoir computing (RC), which achieves classification accuracies of 90.6% and 76.7% for handwritten digit-MNIST and Fashion-MNIST datasets, respectively. These findings highlight that the $VCeO_x$:Ag memristor with a complementary mechanism enables an unprecedented control of analog conductance and paves the way for developing scalable, energy-efficient neuromorphic hardware for edge artificial intelligence (AI) and on-device learning.

Received 1st December 2025,
Accepted 25th February 2026

DOI: 10.1039/d5nr05056a

rsc.li/nanoscale



## Introduction

Neuromorphic computing has emerged as a promising alternative to current von Neumann computing that suffers from low energy efficiency and performance limitations in dealing with vast amounts of data. In addition, it enables efficient implementation of tasks requiring real-time processing of spatio-temporal and time-series data. Since AI and edge computing applications demand highly energy-efficient and scalable hardware emulating biological neural networks, there is a growing interest in hardware-based neuromorphic systems composed of artificial neurons and synapses. Among various emerging devices, memristors with oxide-based resistive random-access memory (RRAM) have gained significant attention as candidates for artificial synapses due to their ability to exhibit analog conductance change, mimicking the weight update of biological synapses. They enable high integration density with a two-terminal structure having a cell size as small as $4F^2$, where F is the minimum feature size, allowing for large-scale and high-density neural network hardware implementations with minimal footprint.

Research efforts have focused on exploring conductance-changing materials and the device structures of memristors to achieve appropriate synaptic properties targeted for a variety of branches in deep neural network (DNN) and spiking neural network (SNN) applications. In any application, the synaptic memristors need to have the common characteristic of tunable conductance at a low operation voltage with high speed. According to the conductance-changing mechanism, the memristor is categorized into either filamentary or non-filamentary type. The filamentary memristor operates through the formation and rupture of conducting filament composed of oxygen vacancies or metal atoms in the conductance- changing materials such as transition metal-oxides,[1–4] two-dimensional[5,6] or three-dimensional chalcogenides,[7,8] Si-

[a]Graduate School of Semiconductor Materials and Devices Engineering, Ulsan National Institute of Science and Technology (UNIST), Ulsan 44919, Republic of Korea. E-mail: tsyoon@unist.ac.kr
[b]Department of Materials Science and Engineering, Ulsan National Institute of Science and Technology (UNIST), Ulsan 44919, Republic of Korea.
E-mail: shinhj@unist.ac.kr
[c]Center for Multidimensional Carbon Materials, Institute for Basic Science (IBS), Ulsan 44919, Republic of Korea

based alloys or compounds,[9–12] and organic layers.[13,14] On the other hand, non-filamentary memristors utilize the migration of oxygen vacancies or metal cations that are distributed within the conductance-changing materials,[15,16] instead of forming conductive filament. The redistribution of oxygen vacancies or metal cations induces the overall conductance to be modulated by changing the energy barrier at the interface with electrodes,[16,17] altering defect (traps) distribution and consequently changing the electron-transport behaviors. Therefore, it is crucial to employ an optimal conductance-changing material in the synaptic memristor having the characteristics of fast migration of oxygen vacancies or metal cations. From the previous research on metal-based filamentary memristors, it has been recognized that metal cations such as silver (Ag) or copper (Cu), have a high mobility in many transition metal-oxides, so they could form filaments at a low operation voltage with a high speed.[18–21] Based on that, it is expected that employing the distribution of active metal cations in a non-filamentary memristor to modulate the analog conductance would be beneficial. To this end, various strategies employing nanocomposite or cluster-embedded thin films have been reported to achieve stable and linear analog switching. For example, designing phase-separated hafnium oxide nanocomposites with Ba-rich nanocolumns has been shown to improve switching uniformity by confining the resistive change to an interfacial barrier.[22] Similarly, effective control over gradual conductance modulation is achieved by engineering cluster-structured filaments within organic matrices[23] or incorporating semiconductor nanoparticles into polymer layers to form nanocomposites.[24] These approaches suggest that incorporating metallic or semiconductor species as discrete clusters or nanocomposite phases within a host matrix is a robust method for mimicking biological synaptic plasticity.

In this study, an Ag-doped vanadium–cerium oxide was employed as a conductance-changing oxide of memristors, where Ag ions were driven to be redistributed under the electric field to modulate the conductance. Moreover, a fraction of doped Ag atoms formed nanoclusters in the vanadium–cerium oxide, thereby facilitating the modulation of conductance in cooperation with ionic redistribution. In our previous study, vanadium oxide ($V_2O_{5-x}$) was verified to be a good medium for Ag-ion migration to form an Ag conducting filament for filamentary memristors.[4] Because the $V_2O_{5-x}$ layer had an amorphous structure with oxygen deficiency, the migration of Ag ions could be facilitated under the electric field. However, because of a narrow bandgap (~2.2 eV) of $V_2O_{5-x}$, it had the drawback of a high off-state current at a high resistance state (HRS), causing a high power consumption.[4,25,26] Also, the high current at HRS would cause the sneak-path leakage current problem in a high-density crossbar array architecture. By comparison, cerium dioxide ($CeO_2$) is also a good medium with a high Ag ion mobility[27–30] and a wider bandgap of ~3.2 eV,[31,32] which could suppress leakage current at HRS. However, it is deposited generally in crystalline form,[30,33,34] causing stochastic and uncontrollable ion migration along randomly distributed grain boundaries.[35,36] Considering these complementary characteristics of $V_2O_{5-x}$ and $CeO_2$, the mixed vanadium–cerium oxide ($VCeO_x$) was employed to achieve high Ag-ion mobility, analog conductance modulation stability, and low HRS leakage current simultaneously.

For the synapse application, it is desirable to modulate the conductance in an analog manner to mimic biological synaptic weight update for neuromorphic computing. In general, it is difficult to achieve analog conductance change *via* controlling filament geometry in a filamentary memristor. For this reason, non-filamentary memristor behaviors were explored through the redistribution of Ag atoms or ions in $VCeO_x$, rather than Ag filament formation. By exploiting the complementary roles of $V_2O_{5-x}$ and $CeO_2$ within the oxide matrix, along with a carefully controlled concentration of doped-Ag species, stable analog conductance modulation was realized while suppressing excessive filament growth. In addition, the temporal response to weight update was used to demonstrate the potential of the device for the application to real-time data processing tasks such as RC applications.

# Experimental

### Device fabrication

As schematically illustrated in Fig. S1, the memristor with a Pt/$VCeO_x$:Ag/Pt structure was fabricated as follows. First, a 70 nm-thick bottom Pt electrode was deposited with a Ti adhesion layer on a $SiO_2$/Si substrate by e-beam evaporation under a base pressure lower than $10^{-6}$ Torr. Then, a $VCeO_x$ layer with a thickness of ~45 nm was deposited by co-sputtering in a radio-frequency (RF) magnetron sputtering system in an Ar atmosphere using high-purity $VO_2$ and $CeO_2$ sputtering targets with a diameter of 2 inches. In the deposition, the base pressure was in the range of $10^{-6}$ Torr, and the working pressure was 20 mTorr. For the Ag doping of the $VCeO_x$ layer, a 3 nm-thick Ag layer was deposited on top of the $VCeO_x$ layer *via* e-beam evaporation and subsequently annealed at 200 °C in vacuum under a pressure lower than 25 Torr to drive Ag atoms into the $VCeO_x$ layer. Finally, a dot-patterned top Pt electrode was deposited by e-beam evaporation using a shadow mask with a diameter of 100 μm. As a reference device, the device without Ag doping, *i.e.*, Pt/$VCeO_x$/Pt memristor, was also fabricated, and its conductance-changing properties were compared with those of the proposed Ag-doped memristor. All fabrication processes were conducted at the maximum temperature of 200 °C, which is compatible with the integration of memristor synapse at the back-end-of-line of the CMOS platform.

### Device measurements

The electrical characteristics of the device, including the analog conductance change by DC voltage sweep, voltage pulse measurements, endurance, and time-dependent modulation of conductance properties, were examined using an Agilent 4156B semiconductor parameter analyzer and a Keithley 4200A-SCS semiconductor parameter analyzer equipped with

 

4225 PMUs. In the measurements, the voltage was applied to the top Pt electrode, while the bottom Pt electrode was grounded.

### Material characterizations

The structure of the device was analyzed using HR-TEM (JEM-2100F, JEOL). The compositions of the $VCeO_x$ layer were examined using EDS (x-Max T-80, Oxford). To evaluate the local surface potential distributions and investigate the electrically induced changes in the work function, KPFM (XE-70, Park Systems) was employed in amplitude-modulated mode under ambient conditions.

### RC simulation

To evaluate the neuromorphic computing capability of the memristor-based physical reservoir system, a classification task was simulated using the MNIST datasets and a 4-bit quantized RC framework. The simulation followed the conventional RC pipeline, consisting of data preprocessing, reservoir state encoding, readout training, and inference.

As an input, 28 × 28 grayscale images of handwritten digit-MNIST and Fashion-MNIST datasets were used with 60,000 images for training and 10,000 for testing. Each image was first binarized using a threshold of 128, converting pixel values to binary (0 or 1). Following binarization, the binary image was reshaped by grouping every four consecutive pixels into a 4-bit segment, resulting in a 196 × 4 binary matrix per image. Each 4-bit group was then converted into a decimal value ranging from 0 to 15 and subsequently mapped to experimentally measured current values corresponding to distinct analog states of the memristor device. This step effectively encoded the quantized input pattern as a 196-dimensional current vector, representing the reservoir state. These current vectors were used as the input to the readout layer, implemented as a single-layer perceptron using PyTorch. The readout model consisted of a BatchNorm1d(196) normalization layer, followed by a fully connected linear layer (196 → 10 nodes). The softmax activation was implicitly handled through the cross-entropy loss function. To train the readout layer, supervised learning was performed using the Adam optimizer with a learning rate of 0.001, a mini-batch size of 100, and a weight decay coefficient of $1 \times 10^{-4}$ to prevent overfitting and enhance generalization. No artificial noise was introduced to the current vector, ensuring consistency with the experimentally measured device characteristics. The input current values were standardized using StandardScaler, centering the data to a zero mean and unit variance prior to training. During training, the model accuracy was monitored on both the training and test sets at each epoch. A batch normalization layer was applied after the 196-node input layer to improve training stability. Final model performance was evaluated based on the epoch that yielded the lowest test loss, and the corresponding predictions were used to generate a confusion matrix. This allowed for class-wise analysis of prediction bias and misclassification patterns.

## Results and discussion

### Analog switching characteristics

Fig. 1 compares the synaptic characteristics of the Ag-undoped device as a reference device ($Pt/VCeO_x/Pt$) and the proposed Ag-doped memristor ($Pt/VCeO_x$:Ag/Pt) under identical voltage and pulse stimuli. Device structure and fabrication processing steps of the $Pt/VCeO_x$:Ag/Pt memristor are schematically illustrated in Fig. 1a and Fig. S1 (SI). The Ag-undoped reference device displays erratic conductance modulation. The current–voltage (*I–V*) sweep curves under repetitive DC voltage sweeps from 0 to +4 V and consequently from 0 to −4 V show a decrease in current during the initial set of sweeps, followed by fluctuating and inconsistent conductance-changing behavior in the subsequent cycles (Fig. 1b). This is also reflected in the conductance values at ±4 V, exhibiting irregular and non-monotonic modulation behavior. In addition, voltage pulse measurements through the application of 64 consecutive square positive pulses of +5 V with a pulse width of 640 μs, followed by 64 negative pulses of −5 V (640 μs), were repeated over five cycles, as shown in Fig. 1c. After each positive and negative pulse, the conductance was read at +1 V (640 μs). As shown in Fig. S2, it was confirmed that the +1 V read operation does not cause any measurable read disturbance during the potentiation and depression cycles. Fig. 1c shows that the current change fluctuates with respect to the pulse application, and there is no consistent polarity-dependent modulation tendency, making the overall behaviors erratic across cycles, similar to the DC *I–V* characteristics observed in Fig. 1b.

In contrast, the proposed Ag-doped memristor ($Pt/VCeO_x$:Ag/Pt) exhibits a markedly improved analog conductance-changing behavior (Fig. 1d). The *I–V* curves in Fig. 1e reveal symmetric and gradual conductance changes dependent on the voltage polarity, *i.e.*, an increase in conductance under positive bias and a decrease under negative bias, demonstrating reliable and repeatable weight updates. The pulse measurements also show consistent behavior (Fig. 1f), obtained by the same procedure shown in Fig. 1c, revealing that the conductance modulates linearly and reversibly with each pulse sequence, maintaining stable potentiation and depression across multiple cycles.

To clearly compare the current change behaviors, the current values from both devices in pulse measurements are presented together in Fig. 1g. The overlaid plot reveals that the Ag-doped memristor exhibits not only an increased overall conductance due to the presence of Ag atoms and nanoclusters in the layer, as will be discussed later, but also significantly stable, linear and symmetric conductance evolution during potentiation and depression. This contrast clearly demonstrates the beneficial impact of Ag doping in $VCeO_x$ on the analog weight update behavior. Such linear and symmetric conductance control is highly beneficial for reliable, energy-efficient, and high-fidelity neuromorphic computations such as training and inference operations, with memristors as artificial synapses.

In this analog conductance change, the conduction in the proposed memristor is verified to be non-filamentary. The

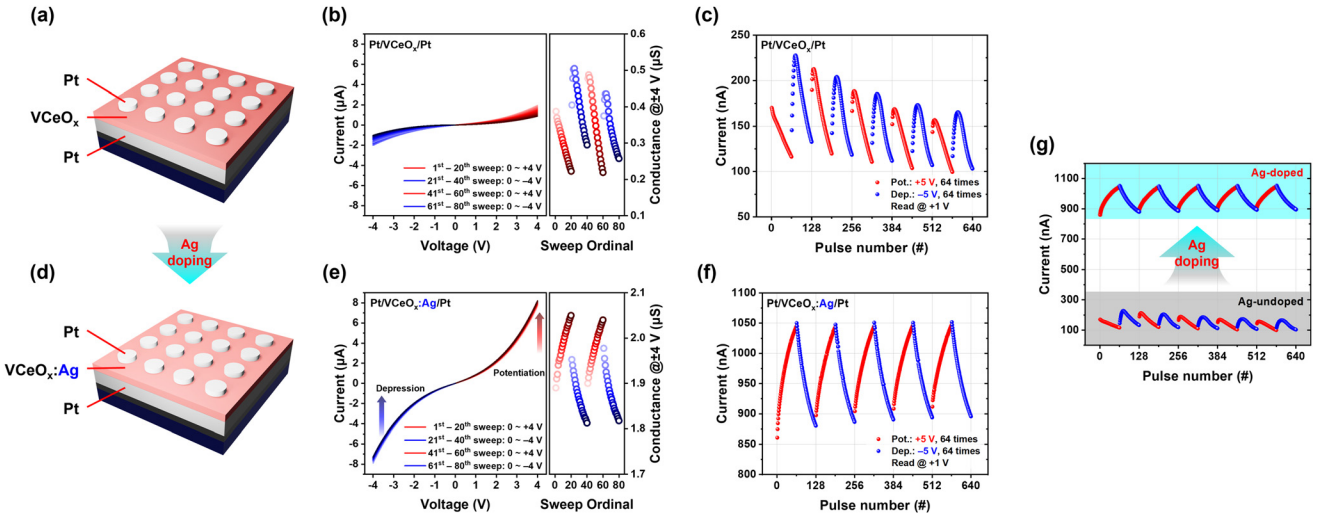


**Fig. 1** (a) Schematic of the Ag-undoped device structure. (b) *I*–*V* curves under repeated bias sweeps and corresponding conductance change at each peak voltage (±4 V). (c) Pulse-induced conductance modulation upon applying +5 V and −5 V pulses (640 μs in width, 64 pulses for each) and read at +1 V, showing erratic inconsistent behavior. (d) Schematic of the Ag-doped device structure. (e) *I*–*V* curves and conductance evolution under identical sweeps, as presented in (b). (f) Pulse-induced modulation under the same conditions as in (c), demonstrating gradual and symmetric conductance changes associated with potentiation and depression with respect to the voltage polarity. (g) Comparison of pulse conductance modulation behaviors between the Ag-undoped and Ag-doped devices (data from c and f, respectively).

measured current at a read voltage of +1 V is approximately 1 μA, which corresponds to the effective filament diameter approximated to be only ~0.29 Å, assuming a metallic Ag filament with a cylindrical geometry and a length equal to the oxide thickness (40 nm) and its resistivity of $1.62 \times 10^{-8}$ Ω m at 25 °C. This is approximately one-tenth the atomic diameter of a single Ag atom (~2.9 Å), suggesting that the analog conductance modulation observed in the device is not governed by the formation of a metallic filament. This conclusion is further supported by the fact that our device operates at significantly lower current levels compared to typical Ag-based filamentary switching, which generally occurs in the hundred-μA to mA range.[4,29,37] Instead, although it needs further verification, the conductance change was induced by the redistribution of Ag atoms. It alters the internal trap states to bridge the transport of electrons, as will be discussed with the aid of the Kelvin Probe Force Microscopy (KPFM) analysis results in Fig. 8.

The operational reliability and stability of the Pt/VCeO$_x$:Ag/Pt memristor under repeated and extended electrical stress conditions were evaluated. Fig. 2 shows the results of the endurance test based on repeating potentiation and depression pulses, cycle-to-cycle (C2C) and device-to-device (D2D) variability. Because the synapse devices experience repeated updates of their weight for computation, the characteristics of fine-tuned weight updates must remain stable over extended operation cycles and across large device arrays.

Fig. 2a presents the endurance characteristics of the device subjected to 300 cycles of alternating potentiation and depression operations. Each cycle consisted of 30 potentiation pulses (+4.5 V, 640 μs), followed by 30 depression pulses (−5 V, 640 μs), amounting to a total of over 18,000 electrical pulses applied throughout the test. The conductance was read under the +1 V read voltage condition. Despite minor stochastic current fluctuations, the overall distinguishable conductance states were well sustained without noticeable degradation throughout the cycling. This level of pulse endurance with reliable and repeatable conductance change during the entire measurement cycles highlights the device's potential for real-time learning (training) and continual weight adjustment without performance loss. The zoomed-in graph shows a magnified view of conductance during cycles 121 to 130 from the endurance dataset. The device exhibits stable and symmetric conductance modulation, preserving the linearity of potentiation and depression characteristics.

The C2C variability of conductance was measured quantitatively over 50 potentiation/depression sequences, each consisting of 30 pulses, as shown in Fig. 2b. The data are visualized *via* a standard box plot, where the interquartile range (IQR) and median provide a quantitative snapshot of the distribution tightness. To account for the occasional stochastic surges observed in endurance tests, conductance values exceeding 860 nS were designated as physical outliers and excluded from the statistical range (as marked in Fig. S3). This confirms a low C2C variability, ensuring that each pulse-induced weight update behaves predictably.

Fig. 2c and d illustrate the D2D variability of the Pt/VCeO$_x$:Ag/Pt memristors. Spatial D2D uniformity was evaluated across 10 randomly selected devices under identical pulsing conditions, consisting of five cycles of 64 pulses at +5 V, followed by 64 pulses at −5 V (640 μs). The corresponding $G_{min}$ and $G_{max}$ values were extracted, and the dynamic range ($G_{max}/G_{min}$) was calculated to examine the spatial fluctuation in conductance modulation. As shown in Fig. 2c, although the absolute

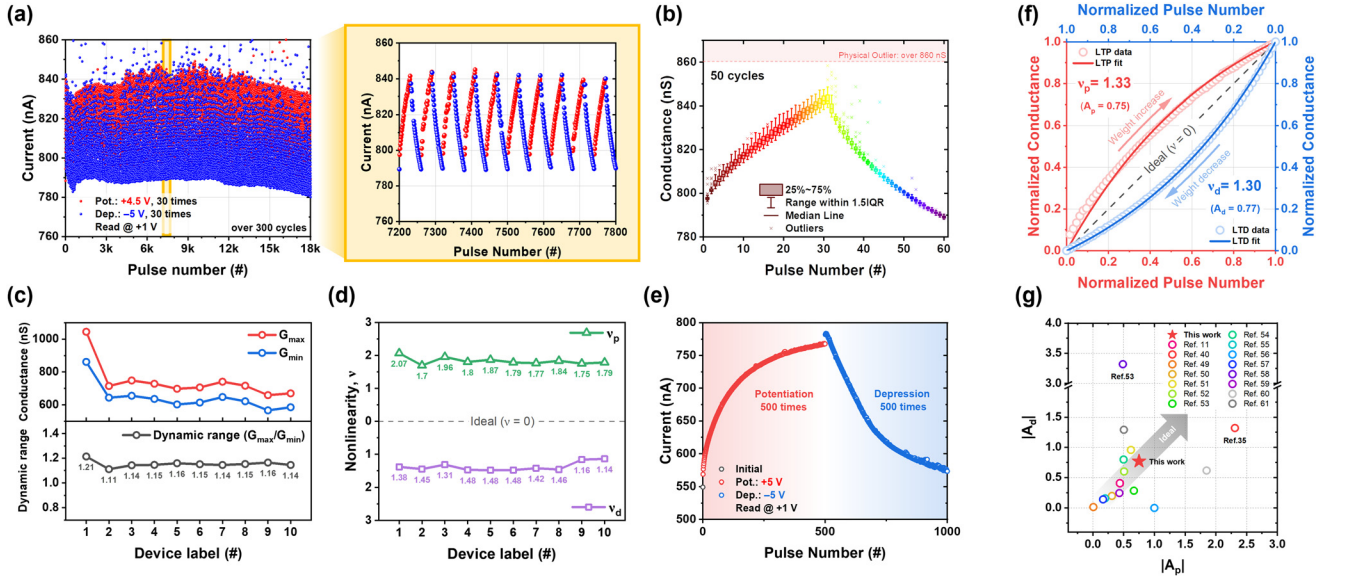


**Fig. 2** (a) Endurance property over 300 potentiation/depression cycles (left) and zoomed-in view of cycles 121–130, highlighting stable potentiation/depression behavior (right). (b) Cycle-to-cycle conductance variation presented as a box plot. (c and d) Device-to-device variability of dynamic range ($G_{max}/G_{min}$) and nonlinearity factor ($\nu$) measured across 10 randomly selected devices, which were used to evaluate spatial fluctuations. (e) Potentiation and depression under 500 consecutive pulses showing high stability. (f) Normalized conductance changes as a function of normalized pulse number during the 5$^{th}$ cycle of potentiation and depression from Fig. 1f, fitted using an exponential nonlinearity model. (g) Linearity benchmark of the Pt/VCeO$_x$:Ag/Pt device with recently reported oxide-based memristor devices.

conductance levels varied between devices to some extent, the $G_{max}/G_{min}$ ratios exhibited a narrow distribution, indicating minimal spatial variability in multilevel conductance modulation. However, the observed dynamic range was relatively limited at approximately 1.1–1.2. While the VCeO$_x$ matrix inherently provides favorable paths for Ag-ion migration, the current range may be constrained by the degree of Ag-ion utilization and the saturation of available switching sites within the matrix. To further enhance this modulation window, future work could focus on maximizing the redox efficiency and ion distribution. Future improvements to expand this modulation window could involve material engineering and redox dynamics optimization, such as adjusting the oxide matrix stoichiometry to create more porous ion-transport paths or incorporating oxidation agents (*e.g.* Pt, Au) to promote Ag ionization.[38] Fig. 2d presents the extracted nonlinearity factors ($\nu$) for potentiation and depression. It presents how the potentiation and depression curves are deviated from the perfect linear condition. Details of the calculation of the nonlinearity factor are described later in the main text of Fig. 2f. It reveals that the devices maintain consistent analog weight update profiles with only minor variations across spatial positions. Even though the ionic redistribution and consequent conductance change are inherently stochastic, these results indicate that the devices yield uniform analog switching characteristics with minimal spatial fluctuation, ensuring reliable performance in neuromorphic systems based on high-density crossbar arrays. Individual conductance evolution curves for each device are provided in Fig. S4.

To further assess the device's capability for achievable analog conductance levels under extended stimulation, the conductance changes by a high number of synaptic pulses, specifically 500 potentiation followed by 500 depression pulses, were measured as shown in Fig. 2e. The conductance increased progressively with the pulse number, showing no abrupt saturation or degradation and enabling access to multiple conductance states up to the measured 500 levels. The device not only sustained its switching behavior over all pulses, but also showed near-linear conductance change in the early phase and fully recoverable states upon depression. This indicates minimal fatigue and further supports the device's capability to function under prolonged, high-frequency synaptic update conditions often encountered during online training phases. Based on this behavior, the additional 700-pulse potentiation data were provided in Fig. S5, which is estimated to support approximately 9-bit resolution. Such high-resolution weight tunability is crucial for analog vector–matrix multiplication tasks in hardware neural networks, where precision and repeatability directly impact inference accuracy. Furthermore, even under the increased bias amplitude of +5 V and repetitive pulse stress, the device maintained stable analog modulation without any abrupt conductance jumps or permanent breakdown. This absence of metallic filament formation, even at higher operating voltages, further confirms the robust non-filamentary nature of the switching mechanism, showing only gradual conductance saturation rather than the discrete state changes typical of filamentary devices.

The Pt/VCeO$_x$:Ag/Pt memristor exhibits a low operation energy consumption of ~9.92 nJ per event during training

(write) and requires only ~0.62 nJ per event during inference (read). Considering the dynamic range of conductance modulation and, consequently, the varied current response at each successive potentiation or depression pulse, the average energy consumption was calculated in the given current range. The detailed energy consumption calculation procedure and results are depicted in Fig. S6. These values are still many orders of magnitude higher than that of the biological ones because they were measured from the device with an electrode diameter of 100 μm. Thus, the scaling-down of the device size to sub-μm ranges would reduce the energy consumption further by several orders of magnitude.

Linearity and symmetry in conductance modulation ensure accurate and predictable weight updates in neuromorphic computation. For the assessment of nonlinearity, several fitting methods have been proposed to evaluate the nonlinearity of the LTP/LTD characteristic curve.[17,39–45] Among them, the method of conductance normalization and fitting with exponential models 1 and 2 were employed:[11,39,46–48]

$$G = G_0(1 - e^{-\nu p}) + G_{\min} \quad (1)$$

$$G = G_{\max} - G_0(1 - e^{-\nu(1-p)}) \quad (2)$$
$$G_0 = (G_{\max} - G_{\min})/(1 - e^{-\nu})$$

Here, $G_{\max}$ and $G_{\min}$ denote the maximum and minimum conductance states, respectively, which are directly extracted from the experimental measurements. The normalized pulse number is defined as $p = P/P_{\max}$, where $P_{\max}$ corresponds to the total number of pulses required to modulate the conductance from $G_{\min}$ to $G_{\max}$ (or *vice versa*). The nonlinearity factor ($\nu$) governs the exponential characteristics of the conductance modulation curves $G_p$ and $G_d$, with its sign and magnitude reflecting the curvature (*i.e.*, convexity or concavity) of the update trajectory. The value of $\nu = 0$ corresponds to an ideally linear response. This formulation enables a clear interpretation of the conductance evolution: larger values of $\nu$ cause rapid saturation toward $G_{\max}$ (or $G_{\min}$), even with a small number of applied pulses. As illustrated in Fig. 2f, the extracted fitting parameters were $\nu_p = 1.33$ and $\nu_d = 1.30$, indicating an almost linear conductance modulation behavior.

For hardware-based artificial neural networks (ANNs), linearity is particularly critical among several required synaptic characteristics, because it directly influences training accuracy and learning stability. To evaluate the linearity of the proposed device in context, its characteristics were compared with those of recently reported memristive synapses through a benchmark graph (Fig. 2g). Since the definition and expression of the nonlinearity factor vary across the literature, where some studies reported it in terms of $\nu$ and others in terms of $A$ (= 1/$\nu$), all reported values were converted into a unified $A$-form for consistent comparison. The extracted nonlinearity parameters of the proposed memristor ($\nu_p = 1.33$, $\nu_d = 1.30$) were accordingly converted into the $A$-form using the relation $A = 1/\nu$. A comprehensive description of the normalization methodology and the reference-by-reference parameter conversions is available in SI Note 1 and Table S1. Compared to previously reported devices,[11,40,49–61] the proposed memristor exhibits competitive conductance linearity, as demonstrated in the benchmark plot presenting larger $A$ values (*i.e.* smaller $\nu$ values) for a more ideal linear behavior.

### Time-dependent synaptic plasticity for RC applications

In addition to the analog conductance-changing characteristics and the demonstration of pattern recognition operation with these properties, time-dependent synaptic characteristics were demonstrated. In biological systems, learning is shaped not only by the strength of connections but also by their temporal response to stimuli, encompassing dynamic processes such as short-term facilitation and spike-dependent memory decay. Fig. 3 highlights the time-dependent synaptic behaviors, including STM associated with a temporary change of the synaptic weight and its transition to LTM with prolonged retention of the updated weight, which collectively govern the processes of learning and forgetting.[62–65]

As time-dependent learning behaviors in neuromorphic systems, learning–forgetting–relearning dynamics were examined under repeated potentiation conditions. This memory formation process can be conceptually understood through classical psychological memory models. According to the multistore model proposed by Atkinson and Shiffrin in Fig. 3a,[62] memory transitions from sensory memory (SM) *via* STM to LTM through attention and rehearsal. Complementarily, the Ebbinghaus forgetting curve[66–68] describes the exponential decay of memory retention over time in the absence of reinforcement, highlighting the critical role of repeated exposure in stabilizing memory traces.

Fig. 3b presents a typical learning–forgetting–relearning behavior under +5 V stimulation. At the initial learning, the conductance increased gradually over the repeated 30 pulses. Then, after a brief decay period, the application of only 11 pulses sufficiently recovered the conductance to the level achieved during relearning, due to the presence of residual memory traces. This reduction in required stimulation for recovering memory is a form of memory facilitation, where prior exposure accelerates subsequent learning. Such behavior mirrors biological memory consolidation, where synaptic traces persist in latent form and enable more efficient reactivation. The requirement of fewer pulses during the relearning stage strongly supports the facilitated relearning behavior of the proposed memristor, mimicking trace-based reinforcement mechanisms in biological synapses.

This qualitative observation is further substantiated in Fig. 3c and d, which track the evolution of conductance over 10 repeated cycles of learning and forgetting behavior. Each cycle involved potentiation, followed by a partial decay phase, allowing the assessment of how the synaptic state evolves under repeated stimulation and intermittent forgetting. In Fig. 3c, each cycle consisted of 30 potentiation pulses (+3 V, +4 V, and +5 V; 640 μs), followed by periodic read operations (+1 V, 640 μs) with a 10 s interval for up to 1 min to monitor short-term retention and natural decay. The application of higher pulse amplitudes produced larger conductance increase and

 

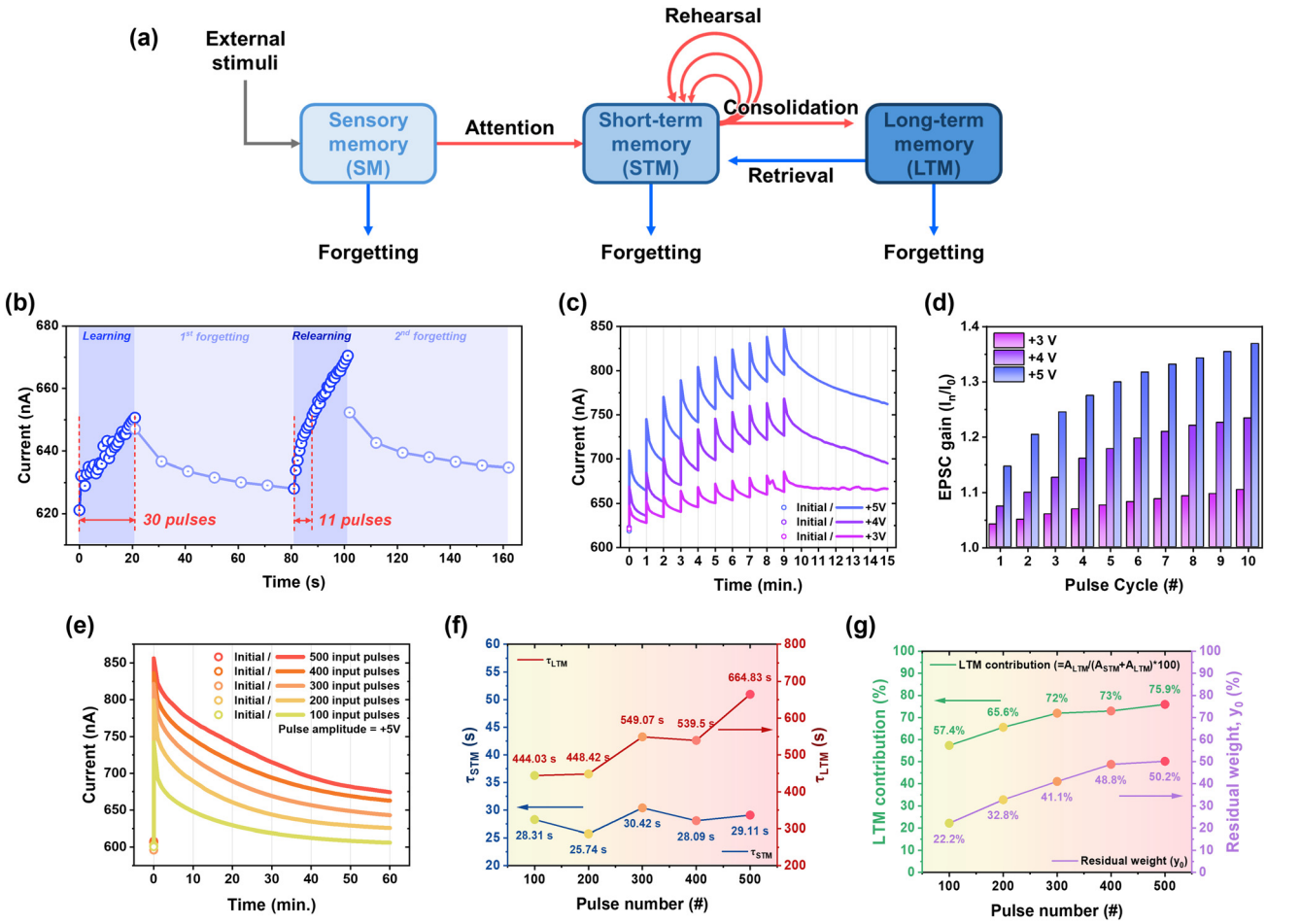


**Fig. 3** (a) Schematic of the psychological multi-store memory model proposed by Atkinson and Shiffrin.[62] (b) Pulse-driven learning–forgetting–relearning dynamics measured under +5 V pulses, illustrating faster conductance recovery during relearning compared to that during the initial learning. (c) Repeated learning–forgetting cycles under different pulse amplitudes (+3 V, +4 V, and +5 V). (d) Extracted EPSC gain after each learning cycle in c, demonstrating spike-amplitude-dependent plasticity (SADP). (e) Multilevel conductance modulation and retention characteristics after applying 100, 200, 300, 400, and 500 pulses (+5 V, 640 μs), followed by 60 min of read operations with 1 min interval. (f) Extracted short- and long-term decay constants ($\tau_{STM}$ and $\tau_{LTM}$) from the initial 10 min decay segment fitted with a double exponential decay function. (g) Evolution of LTM contribution and residual synaptic weight, demonstrating enhanced memory consolidation with increasing pulse count.

more persistent memory traces, demonstrating spike-amplitude-dependent plasticity (SADP). Notably, successive cycles exhibited progressive increase in final conductance, suggesting successful relearning behavior and cumulative potentiation despite intermittent forgetting. To quantitatively analyze this cumulative potentiation, the normalized excitatory postsynaptic current (EPSC) gain ($I_n/I_0$) was extracted for each cycle and plotted in Fig. 3d. As the pulse amplitude increased, the cycle-wise EPSC gain rose more steeply with each cycle, confirming the voltage-amplitude dependency in synaptic potentiation. Higher pulse amplitudes resulted in stronger initial learning, more persistent memory traces, and more efficient relearning. This trend parallels biological synapses, where stronger presynaptic stimuli facilitate more robust memory encoding and faster recovery upon re-exposure, reflecting a form of stimulus-dependent memory consolidation. These results illustrate how prior stimulation history and input amplitude jointly modulate the learning speed and retention, capturing multiple aspects of biological memory dynamics.

To further investigate the plasticity timescale, the conductance evolution after applying different numbers of potentiation pulses (100–500) at +5 V (640 μs) was examined. As shown in Fig. 3e, the conductance increased proportionally with a pulse count and subsequently decayed over time. Smaller repetition number of stimulations resulted in faster decay, while prolonged stimulation with a larger repetition number led to more sustained retention, indicating a transition from STM to LTM. Despite partial retention loss, the device maintained distinguishable conductance levels, enabling multilevel state encoding. In particular, this STM-to-LTM transition enables the device to encode memory strength as a function of stimulation duration, effectively capturing both the intensity and temporal structure of the presynaptic activity. Such behavior provides a hardware-level analogy of

memory consolidation, a fundamental process in biological synapses that stabilizes transient synaptic changes into LTM.

This STM-to-LTM transition was quantitatively analyzed by fitting the initial 10 min segments of the retention curves in Fig. 3e after normalizing to the range of 0 to 100, with a double exponential decay function in the form of $y = A_1 \cdot \exp(-t/\tau_1) + A_2 \cdot \exp(-t/\tau_2) + y_0$, where $A_1$ and $\tau_1$ represent the amplitude and time constant associated with the STM component with fast decay at the early stage, respectively, and $A_2$ and $\tau_2$ correspond to the LTM component with slow decay at the following stage. Hereafter, $A_1$ and $A_2$ are denoted as $A_{STM}$ and $A_{LTM}$, and $\tau_1$ and $\tau_2$ as $\tau_{STM}$ and $\tau_{LTM}$, respectively. The offset $y_0$ accounts for the residual synaptic weight retained after prolonged decay, representing the consolidated portion of memory that persists beyond transient and short-term components. Fitting the given retention curve with a double exponential decay function separates the STM and LTM components in the decay characteristics. Detailed fitting results, including the original retention data and the corresponding double-exponential curves with extracted parameters, are provided in Fig. S7. As shown in Fig. 3f and g, the fast decay constant $\tau_{STM}$ remained relatively unchanged with increasing pulse number, indicating that the dynamics of STM were not significantly affected by the stimulation count. In contrast, the slow decay constant $\tau_{LTM}$ exhibited a clear upward trend with increasing pulse number, suggesting enhanced stability and persistence of the LTM component. Furthermore, the relative contribution of the LTM component, defined as $A_{LTM}/(A_{STM} + A_{LTM}) \times 100$, also increased monotonically, confirming that repeated stimulation facilitates memory consolidation by progressively shifting the balance from short-term to long-term retention. The residual synaptic weight $y_0$, which quantifies the final retained memory level after both exponential decay processes have settled, also increased with the pulse count. This further supports the emergence of consolidated memory states that remain distinguishable even after extended idle periods.

The temporal dynamics of the Pt/VCeO$_x$:Ag/Pt memristor were further explored by examining the SRDP and PPF characteristics. As shown in Fig. 4a, a series of 10 consecutive pulses (+5 V, 640 μs) was applied while reducing the inter-spike interval ($\Delta t$) from 20 to 0.5 s. Each spike event was followed by a wait period, *i.e.*, the designated interval. Then, the decayed conductance was measured for 400 s. The EPSC increased with the decrease in the interval, demonstrating a typical SRDP behavior in which rapid firing enhances synaptic efficacy. This increased conductance by SRDP is quantitatively visualized in Fig. 4b. The EPSC peaks increase more steeply under shorter intervals, consistent with biological synapses where higher spike rates lead to stronger postsynaptic responses.

Short-term synaptic facilitation behavior was examined by evaluating the PPF index as a function of the inter-spike interval, as shown in Fig. 4c. The PPF is a representative feature of short-term synaptic plasticity, wherein the postsynaptic current in response to the second stimulus is enhanced when it follows closely after the first. This phenomenon arises from the residual calcium ion ($Ca^{2+}$) dynamics in biological

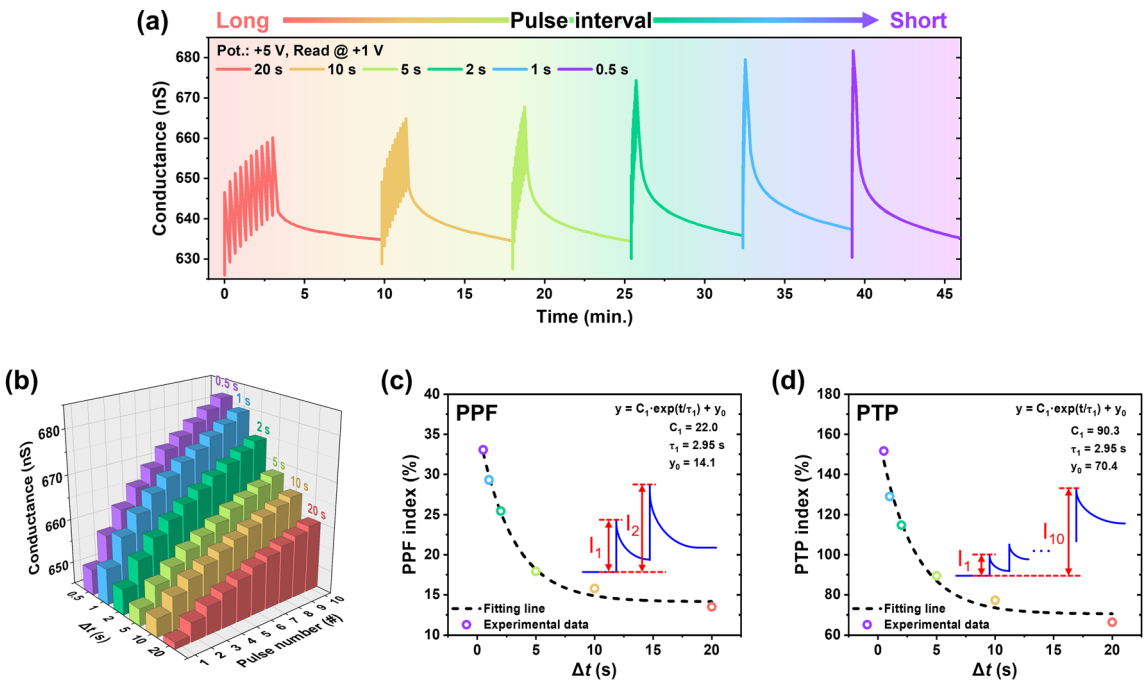


**Fig. 4** (a) EPSC evolution under different inter-spike intervals ($\Delta t$, 0.5–20 s) during a 10-cycle spike stimulation (+5 V, 640 μs), mimicking SRDP in biological synapses. (b) Peak EPSC values as a function of pulse number and $\Delta t$. (c) PPF index as a function of $\Delta t$ between two consecutive pulses and fitted curve (dotted line). (d) PTP index as a function of $\Delta t$ between a train of ten consecutive presynaptic pulses, calculated by comparing first and tenth EPSC.

synapses and serves as a fundamental mechanism for temporal information processing. The observation of the PPF behavior in the device indicates its capability to capture short-term temporal correlations between consecutive inputs. Such temporal responsiveness replicates brain-like functions, including temporal summation, sensory filtering, and STM in recurrent neural network (RNN) architectures. The PPF index presents quantitatively the relative enhancement of EPSC in response to two consecutive pulses, defined to be $((I_2 - I_1)/I_1) \times 100$, where $I_1$ and $I_2$ denote the EPSC amplitudes following the first and the second pulses, respectively. To analyze the interval dependence of the index, the PPF curve was fitted with an exponential decay function, as shown in eqn (3):

$$y = C_1 \cdot \exp\left(-\frac{t}{\tau_1}\right) + y_0 \quad (3)$$

where $\tau_1$ represents the characteristic relaxation time, $C_1$ denotes the initial facilitation amplitude, and $y_0$ corresponds to the saturated facilitation level at longer intervals. This unimodal decay profile suggests a dominant relaxation pathway (Fig. 4c and Fig. S8).

While biological synapses frequently exhibit double exponential decay due to the coexistence of fast and slow relaxation components,[55,69–72] previous studies have also demonstrated that a single exponential model can effectively capture the essential dynamics of short-term plasticity (STP) when a single time constant dominates the response.[72,73] In the proposed memristor, the PPF index decreased exponentially with increasing $\Delta t$, starting from a maximum of 33% at $\Delta t$ = 0.5 s and gradually approaching approximately 13.5% at longer intervals. This temporal response closely resembles the function of biological synapses to decode temporal patterns of sensory inputs such as visual and auditory signals, within specific frequency domains.[75,76] Notably, the extracted time constant, $\tau_1$ = 2.95 s, falls within the biologically relevant timescale for information processing, typically on the order of hundreds of milliseconds to a few seconds.[77] The ability to reproduce the characteristic features of PPF observed in biological systems underscores its potential for implementing time-dependent neural computations in neuromorphic hardware while preserving modeling simplicity and interpretability.

In addition, PTP, another representative form of STP, was examined. While PPF reflects transient synaptic enhancement triggered by two closely spaced input spikes, PTP captures more prolonged facilitation resulting from the cumulative effect of repetitive stimulation over a relatively extended period. Despite their differences in temporal duration and induction protocols, both characteristics have decisive roles in short-term information retention and dynamic filtering of temporally correlated inputs in biological and artificial neural systems. The PTP index was similarly defined as $((I_{10} - I_1)/I_1) \times 100$, where $I_1$ and $I_{10}$ represent the EPSC amplitudes measured after the first and the tenth pulses, respectively. As depicted in Fig. 4d, the EPSC amplitude increased cumulatively with repeated stimulation, demonstrating a prolonged synaptic enhancement that gradually saturated after multiple pulses. The PTP index curve with respect to inter-spike interval was also fitted with the exponential decay function, similar to the PPF index curve. The coexistence of PPF and PTP confirms that the proposed memristor emulates a broad spectrum of short-term synaptic plasticity, enabling biologically relevant, frequency-dependent memory behavior for spike-timing-based neuromorphic processing.

The performance of the proposed Pt/VCeO$_x$:Ag/Pt memristor was contextualized through a benchmark comparison with previously reported artificial synapse devices featuring metal-embedded switching matrices, as presented in Table S2. Key parameters including the device structure, embedded metal species, and synaptic functionalities (such as conductance dynamic range, switching linearity, endurance, and neuromorphic properties), are compared. While many prior studies have focused on improving either switching endurance, multilevel precision, or time-dependent plasticity, separately, the proposed device uniquely achieves all of these traits in a single platform. Specifically, it exhibits exceptionally high analog linearity and symmetric conductance modulation, along with robust pulse endurance exceeding $10^4$ pulses and fine-grained multilevel conductance resolution up to approximately 9-bit precision. Furthermore, it successfully emulates a diverse range of biologically relevant synaptic behaviors, including PPF, PTP, SRDP, SADP, STM-to-LTM transition, and fading memory, which demonstrate its capacity to mimic both temporal and structural aspects of synaptic learning.

The feasibility of the Pt/VCeO$_x$:Ag/Pt memristor in hardware-level temporal processing was explored through an RC framework implemented using experimentally measured device characteristics. The RC leverages the inherent dynamics and fading memory of physical systems, here, with time-dependent conductance change in the memristor, to perform temporal encoding with only the readout layer being trained. This paradigm offers computational advantages by minimizing training complexity while maintaining high representational power.

Fig. 5a presents a schematic overview of the reservoir computing architecture, comprising an input layer, a nonlinear reservoir layer, and a readout layer. Fig. 5b illustrates the implemented system in detail. For the image-preprocessing, handwritten digit-MNIST and Fashion-MNIST images (28 × 28) were first binarized and rearranged *via* column-wise 4-bit grouping, producing a 196 × 4 matrix. These binary matrices were mapped to quantized input currents through 4-bit pulse encoding schemes, effectively translating spatial image information into temporal input sequences suitable for reservoir processing.

The reservoir layer consisted of 196 memristor devices, each receiving a unique pulse stream based on the input encoding. The intrinsic temporal dynamics and fading memory of the memristor enabled it to transform incoming pulses into high-dimensional conductance states that collectively form a nonlinear reservoir representation. The response of each device at the end of the pulse stream, *i.e.*, the final current state after the

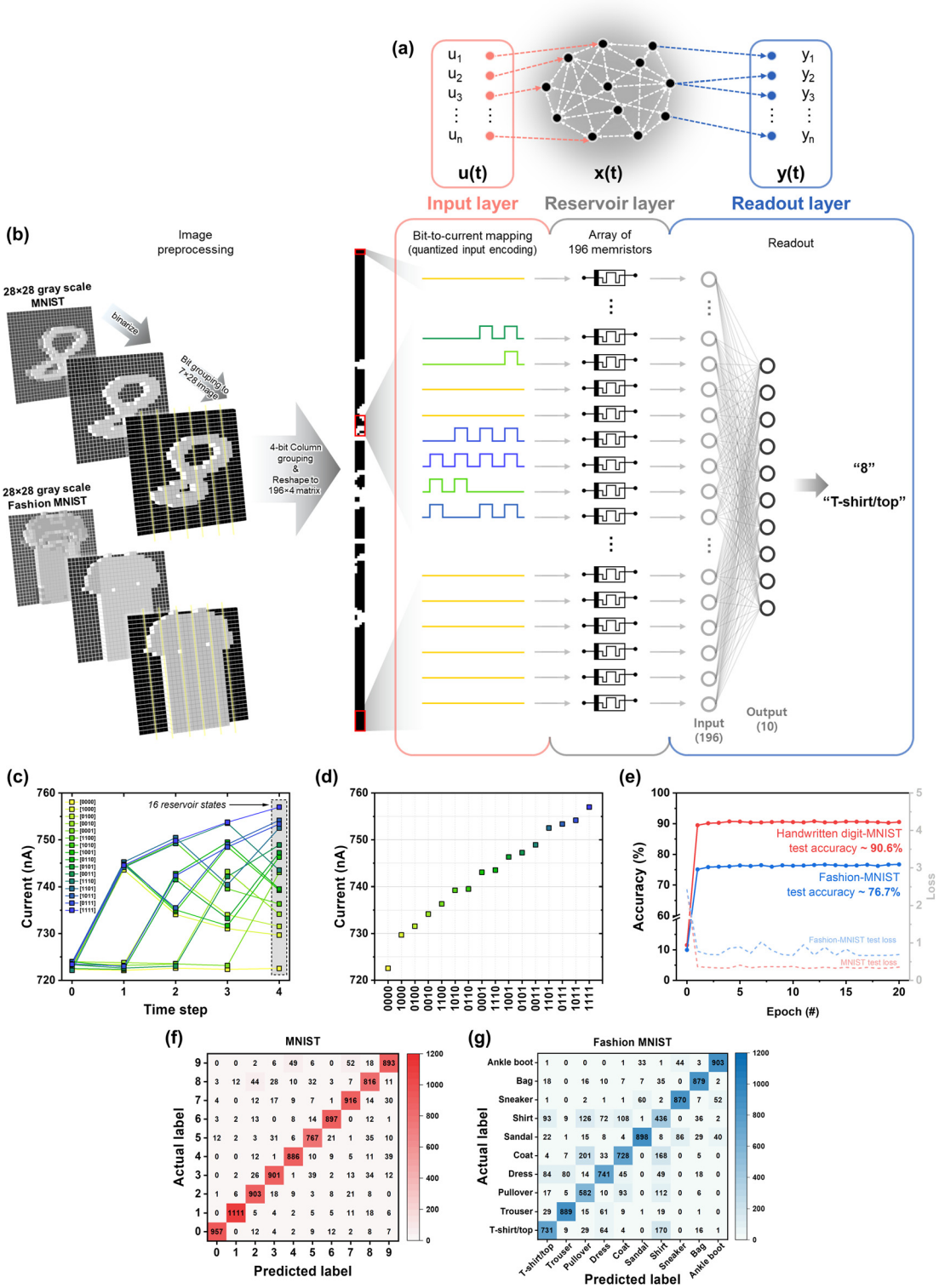


**Fig. 5** (a) Schematic of a conventional RC architecture, consisting of an input layer, a nonlinear reservoir layer with fixed random internal connections, and a trainable readout layer. (b) Flow schematic of the simulation for handwritten digit-MNIST and Fashion-MNIST image classification using the proposed RC system. (c) Measured current responses of the Pt/VCeO$_x$:Ag/Pt memristor to 16 distinct 4-bit binary pulse streams. (d) Final-state current levels corresponding to 16 reservoir states, demonstrating the separability of reservoir states. (e) Recognition accuracy and loss trends for handwritten digit-MNIST and Fashion-MNIST classification tasks using the memristor-based RC system and (f and g) their confusion matrices.

pulse stream, was used as the reservoir state. The readout layer employed a single-layer perceptron (SLP) with 196 inputs and 10 output classes. This configuration reflects the core principle of RC: complex nonlinear and temporal transformations are handled by the reservoir, while the readout performs a simple linear classification. This design ensures fast training, reduced parameter overhead, and efficient inference. Detailed simulation procedures are provided in the Experimental section.

The device's suitability for reservoir-based encoding was validated as shown in Fig. 5c. It presents the memristor's electrical responses as a form of the final current values to a full set of 4-bit binary pulse streams representing 16 distinct input states, ranging from [0000] to [1111]. To provide a more detailed view of each response trajectory, the temporal current profiles corresponding to each 4-bit pulse stream ([0000] to [1111]) are provided separately in Fig. S9. Each 4-bit sequence was applied to the device as a temporally encoded pulse stream, where one time step corresponds to one bit position. At every time step, a +1 V read pulse (640 μs) was applied. If the bit at that position was '1', a +5 V programming pulse (640 μs) preceded the read pulse; if the bit was '0', only the read pulse was applied. An inter-step delay of 1 s was introduced to utilize the device's intrinsic fading memory characteristics. For example, the input [0101] corresponds to four sequential time steps in which the device experiences: (1) read-only, (2) program & read, (3) read-only, and (4) program & read. The resulting current profiles exhibit consistent and distinguishable trends across the 16 input cases, confirming the memristor's ability to resolve temporally structured pulse streams and effectively encode them into unique reservoir states.

Notably, the conductance evolution for each input pulse stream exhibits highly consistent incremental and decaying slopes across corresponding time steps, as illustrated in Fig. S10. For instance, in the case of state sequences, such as [1000], [0100], [0010], and [0001], the initial potentiation at the respective activation step yields nearly identical current increases (Fig. S10a). Similarly, multi-bit states like [1100], [0110], and [0011], which share analogous temporal structures with two sequential activations, exhibit reproducible current slopes at equivalent activation steps (Fig. S10b and c). This slope clustering behavior indicates that the conductance modulation is not solely governed by the total number of programming pulses, but also closely linked to the temporal alignment of input events. In other words, memristive response patterns become consistently shaped when the relative activation sequences are aligned, resulting in structured and repeatable temporal conductance trajectories. Such time-dependent regularity enhances the separability of reservoir states, facilitating reliable mapping of temporally encoded input sequences. This predictable behavior is particularly advantageous for neuromorphic tasks involving RNNs, where precise temporal transitions and the retention of sequential input history are critical. The observed consistency across analogous activation patterns yields stable and state-dependent dynamics, providing a robust and physically grounded substrate for implementing RNN-inspired processing architectures.

Fig. 5d summarizes the final current responses extracted after applying each of the 16 unique 4-bit pulse streams, showing the discriminative capability of the memristor-based reservoir. Despite some degree of overlap among closely spaced input cases, the overall current distribution is revealed to separate the 16 states, enabling reliable classification in the subsequent readout stage.

Following the simulation framework outlined in Fig. 5b, the experimentally derived reservoir states were used for image classification tasks. As shown in Fig. 5e, the model's performance was evaluated over 20 epochs by monitoring both accuracy and loss. In the figure, the solid lines represent the classification accuracy, while the dashed lines indicate the corresponding loss values. For the handwritten digit-MNIST and Fashion-MNIST datasets, the test accuracies of 90.6% and 76.7% were achieved, respectively. As the model's accuracy progressively increased, the loss consistently decreased over the training epochs, confirming a stable learning process. This performance in processing spatiotemporal features originates from the memristor's inherent time-decaying behavior. The gradual and state-dependent conductance relaxation naturally implements a fading memory effect, which enables the encoding of temporal input history. By leveraging this dynamic behavior, the system successfully projects input streams into a high-dimensional space that retains relevant spatiotemporal information, thereby enabling efficient and accurate classification with minimal training overhead.

Fig. 5f and g illustrate the confusion matrices obtained from handwritten digit-MNIST and Fashion-MNIST classification tasks, respectively. Each row represents the ground-truth label (actual input label), and each column shows the predicted label obtained through RC; the diagonal values, therefore, quantify correct recognitions, whereas off-diagonal entries present specific misclassifications. In the handwritten digit-MNIST task (Fig. 5f), the overall classification accuracy exceeded 90%, indicating negligible pairwise confusion between digit classes. On the other hand, the Fashion-MNIST matrix (Fig. 5g) exhibits some off-diagonal clusters. For example, there are misclassifications of "Coat" to "Pullover" with 17.5% of total 'Coat' predictions, "T-shirt/Top" to "Shirt" with 16.6% of total 'T-shirt/Top' predictions, and "Coat" to "Shirt" with 14.7% of total 'Coat' predictions. These categories share similar silhouettes or textures in grayscale images, so they are frequently confused even in software benchmarks. Nevertheless, all main-diagonal values remain above 76%, confirming that the reservoir states generated by the Pt/VCeO$_x$:Ag/Pt memristor retain sufficient class-specific information for reliable inference while revealing the dataset-intrinsic ambiguities. All of these results validate the proposed memristor's potential for RC that can achieve high classification accuracy using minimal training complexity and a simple linear readout architecture.

### Material characterizations and conductance-changing mechanism

To elucidate the structural characteristics and conductance-changing mechanism of the Pt/VCeO$_x$:Ag/Pt memristor, high-

resolution transmission electron microscopy (HR-TEM) analysis was performed on both the Ag-undoped reference device (Pt/$VCeO_x$/Pt) and the proposed Ag-doped memristor (Pt/$VCeO_x$:Ag/Pt). As shown in Fig. 6a and b, the $VCeO_x$ matrix maintained a highly uniform amorphous structure irrespective of Ag doping, which is advantageous for achieving device-to-device uniformity in conductance change. In addition, energy-dispersive X-ray spectroscopy (EDS) analysis revealed that the V/Ce atomic ratio in the $VCeO_x$ matrix was approximately 1.5 (V : Ce = 1.5 : 1). The compositional profiles obtained from the EDS line scans for each device are presented in Fig. S11. These profiles also confirm that the deposited Ag thin film was completely dissolved and uniformly distributed throughout the $VCeO_x$ matrix during the annealing process, as no significant accumulation or residual metallic Ag layer was observed at the electrode interface. Furthermore, the interface between the $VCeO_x$:Ag layer and the top Pt electrode appeared flat, owing to the amorphous nature of the $VCeO_x$:Ag layer, since amorphous phases inherently exhibit lower surface roughness compared to their polycrystalline counterparts.[78–80] It can also be confirmed by atomic force microscopy (AFM) results of the $VCeO_x$:Ag layer (Fig. S12) and scanning electron microscopy (SEM) images of layers with varying V/Ce compositions (Fig. S13). They show that pure $VO_x$ has a featureless and amorphous surface morphology, while $CeO_2$ forms a polycrystalline structure with pronounced grain boundaries. In contrast, the $VCeO_x$ layers retain the smooth and amorphous microstructure, effectively combining the advantages of each oxide component.

In the pristine Pt/$VCeO_x$:Ag/Pt memristor (Fig. 6b), uniformly distributed Ag nanoclusters (~2–3 nm in diameter) were clearly observed within the amorphous matrix. Upon electrical stimulation with 500 times of +5 V pulses (640 μs) applied to the top electrode, these Ag clusters were enlarged, as shown in Fig. 6c. The red-dotted region, highlighting this enlarged cluster, is further magnified in Fig. 6d, where lattice fringes corresponding to an interplanar spacing ($d$) of 2.13 Å match well with the (200) planes of face-centered cubic (fcc) Ag. It indicates that the Ag clusters were embedded within the amorphous $VCeO_x$ matrix and enlarged upon repeating bias application, most probably resulting from Ag-ion migration under the electric field. To further investigate the reversibility of this structural evolution, additional bias-dependent TEM analysis was conducted (Fig. S14). While the clusters are found to undergo the changes in their size resulting from Ag-ion

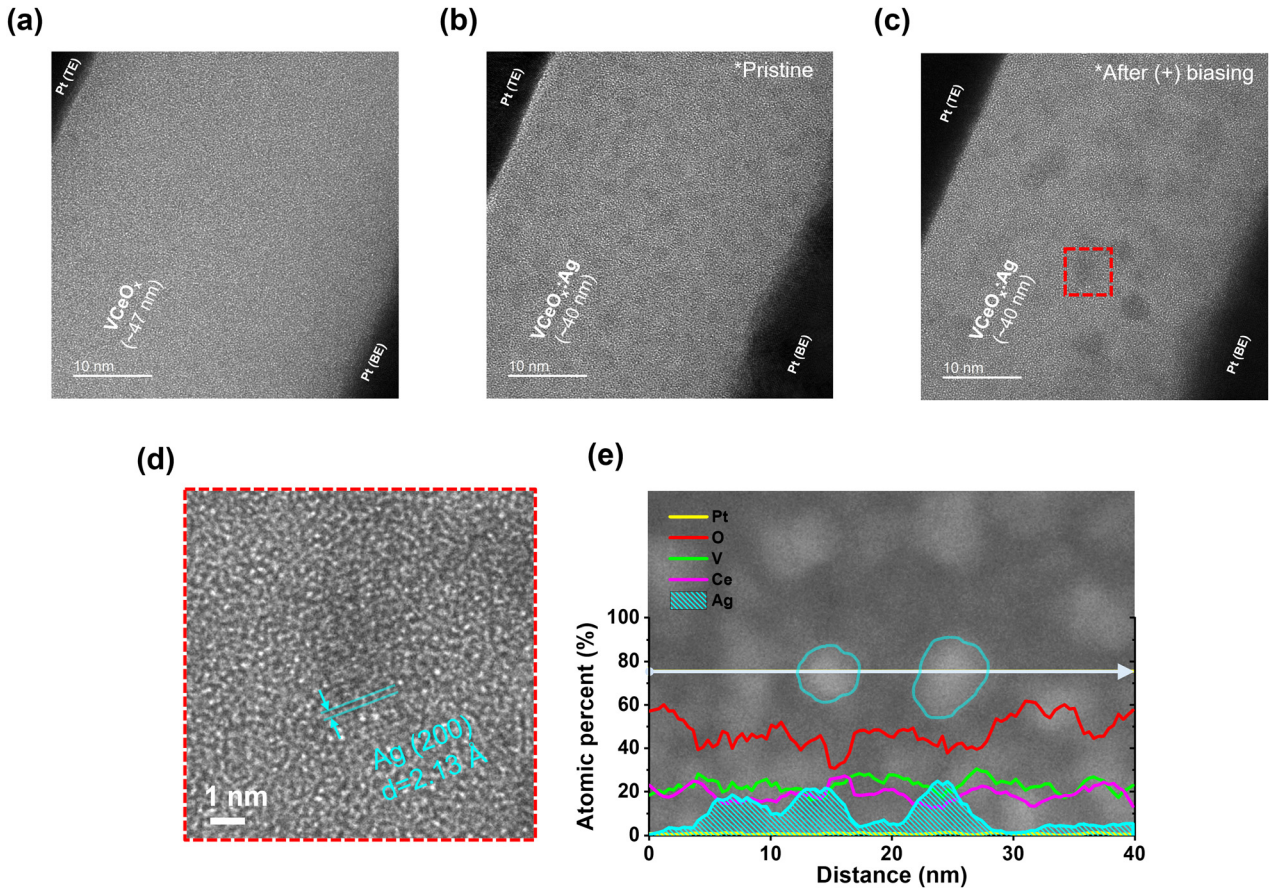


**Fig. 6** (a–c) Cross-sectional HR-TEM images of the Ag-undoped reference device (Pt/$VCeO_x$/Pt) and the proposed Ag-doped memristor (Pt/$VCeO_x$:Ag/Pt): (a) Ag-undoped reference device, (b) Ag-doped memristor in the pristine state having distributed Ag nanoclusters, and (c) Ag-doped memristor after potentiation *via* 500 pulses at +5 V (640 μs), showing the presence of enlarged clusters. (d) Magnified HR-TEM image of the red-dotted region in (c), confirming the cluster to be made of Ag atoms. (e) EDS line-scan analysis of the Ag-enriched regions in the $VCeO_x$:Ag layer.

migration upon repeated bias application, they did not grow abnormally. Crucially, these subtle structural variations do not lead to electrical degradation, as confirmed by the stable endurance (Fig. 2a) and repeatable weight update characteristics (Fig. 2e), even under extensive electrical stress. EDS line scanning performed across the cross-section of the memristor structure (Fig. 6e) confirmed the presence of Ag-rich regions corresponding to the nanoclusters.

Based on the previous electrical characteristics and TEM analysis, the conductance-changing mechanism of the Pt/$VCeO_x$:Ag/Pt memristor is suggested in Fig. 7. While diverse conductance-changing mechanisms have been proposed, the conductance change in memristors with embedded metal nanoclusters broadly falls into two commonly discussed categories: (i) conductive metallic bridge modulation[37,41,81,82] and (ii) charge storage and release (charging/discharging) dynamics from the metal nanoclusters.[74,83] However, the conductance-changing characteristics of the proposed device in this study do not align with either mechanisms. First, the measured current levels are too low to be attributed to conductive filaments. If a filament existed, its calculated diameter would be an order of magnitude smaller than that of a single Ag atom, rendering filamentary conduction physically implausible, as discussed in the context of Fig. 1. Second, the observed polarity-dependent potentiation and depression behaviors are incompatible with charge-based modulation in a symmetric two-terminal structure, where voltage polarity typically does not affect.

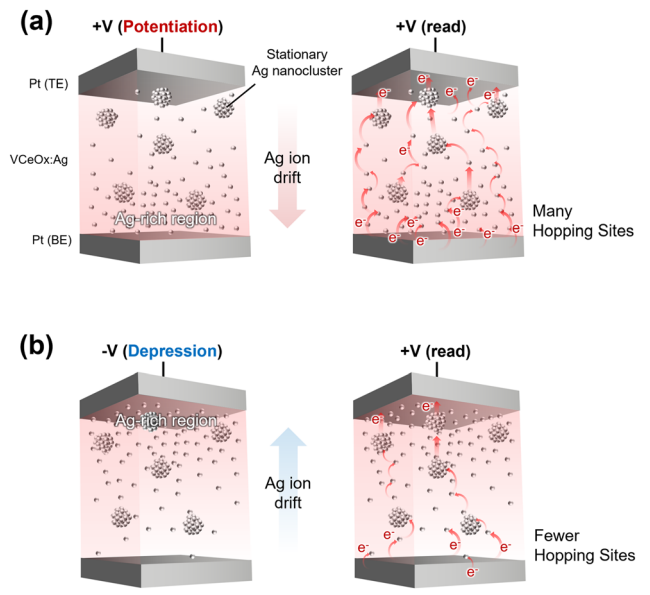


**Fig. 7** Schematic of the proposed conductance-changing mechanism in the Pt/$VCeO_x$:Ag/Pt memristor based on the field-driven modulation of atomic-scale Ag hopping sites. (a) During potentiation, $Ag^+$ species redistribute toward the bottom electrode, forming a dense Ag-rich region that increases the availability of localized hopping sites. Electron conduction is facilitated *via* quasi-stationary Ag nanoclusters acting as fixed tunneling bridges, enhancing the probability of percolative hopping pathways. (b) During depression, $Ag^+$ species migrate toward the top electrode, reducing the hopping site density in the bottom region and thus impeding electron transport.

Instead, a new conduction model is proposed, wherein atomic-scale, mobile $Ag^+$ species migrate under the influence of an external field and modulate the density of localized hopping sites in the $VCeO_x$ matrix. In this model, the embedded Ag nanoclusters act as quasi-stationary tunneling anchors, facilitating electron transport *via* multiple hopping events. The spatial configuration of $VCeO_x$:Ag with an Ag nanocluster resembles a granular metal–insulator system, where fixed metallic islands promote field-assisted hopping across a disordered host matrix.[84–87] During potentiation, positively biased conditions induce field-driven redistribution of $Ag^+$ species toward the bottom interface, thereby increasing the density of localized hopping sites in that region, as illustrated in Fig. 7a. In this context, the presence of quasi-stationary Ag nanoclusters provides intermediate metallic domains that bridge otherwise disconnected regions, enabling electron transport *via* a sequence of field-assisted tunneling and hopping transitions across the amorphous $VCeO_x$ matrix. If these nanoclusters were absent, *i.e.*, when only redistributed atomic-scale $Ag^+$ species were present, the resulting hopping site distribution would be spatially imbalanced. Although site density would increase near the bottom electrode, a simultaneous depletion of hopping sites near the top electrode disrupts the continuity of the percolation network. As a result, electron conduction across the entire layer would be significantly less efficient, limiting the potentiation effect.

Conversely, during depression, the application of a negative bias drives Ag ions to redistribute toward the top interface, progressively depleting the density of available hopping sites near the bottom electrode (Fig. 7b). Although the embedded Ag nanoclusters remain stationary and continue to function as intermediate tunneling anchors, the decrease in carrier injection from the bottom electrode due to the depletion of $Ag^+$ species leads to a reduced probability of electron conduction. In this case, conduction is no longer limited by the bridging function of the nanoclusters, but rather by the diminished population of accessible hopping sites that can feed electrons into the percolation network. This spatial redistribution leads to suppressed electron conduction, consistent with the experimentally observed depression behavior. Taken together, this hypothesis explains both the asymmetric conductance modulation with respect to voltage polarity and the continuous analog conductance tuning observed in the device. A key factor in this polarity-dependent switching is that the device conductance is predominantly governed by the interfacial state near the bottom electrode under the fixed read voltage polarity (positive bias at the top electrode). Under this condition, the accumulation of Ag ions near the bottom interface during potentiation significantly enhances electron injection and transport, facilitated by the synergy with stationary Ag nanoclusters. While the top interface becomes depleted of mobile ions, it does not become an absolute bottleneck because the large amounts of injected electrons could move through the embedded Ag nanoclusters, acting as quasi-stationary tunneling anchors, or be excited to the conduc-

tion band and migrate under the electric field. On the other hand, during depression, Ag ions are depleted from the bottom interface. As a result, the amount of injected electrons would be significantly reduced at the same positive read voltage condition. It would result in increased resistance as a depression, whose schematics are illustrated in Fig. S15. This mechanism interprets polarity-dependent potentiation and depression behaviors with the redistribution of Ag ions, which is also confirmed from the KPFM analysis that is discussed in the following section.

Regarding Ag-ion redistribution, it is important to consider the thermodynamic solubility of Ag in the $VCeO_x$ matrix, which critically governs the coexistence of mobile atomic-scale species and quasi-stationary nanoclusters. If the solubility is too high, Ag would remain fully dispersed at the atomic level, making cluster formation unlikely and thereby undermining the tunneling-anchor-assisted conduction mechanism described in Fig. 7. Conversely, if the solubility is too low, Ag atoms would precipitate entirely into metallic aggregates, eliminating the reservoir of residual atomic Ag necessary for conductance modulation. Although the solubility data are not available, a certain amount of Ag atoms are thought to be dissolved in these oxides, verified from the results of Ag-filamentary RRAM involving the dissolution of Ag atoms in the oxides as a route for Ag filament formation in the oxides.[4,30] The coexistence of both stationary nanoclusters and dynamic residual $Ag^+$ species forms the basis for the subsequent bias-driven ionic redistribution and consequent conductance-changing behaviors. The presence of mobile atomic-scale $Ag^+$ species will be further investigated using KPFM in the following sections.

To elucidate the presence and dynamic behavior of mobile $Ag^+$ species in the $VCeO_x$:Ag layer, KPFM analysis was performed, as summarized in Fig. 8. KPFM offers high-resolution mapping of local electronic properties by exploiting its inherent sensitivity to work function variations at the nanoscale. It functions by detecting electrostatic forces between an AFM tip and the sample surface and determining the contact potential difference (CPD), which arises from the difference in work function between the conductive AFM tip ($\phi_t$) and the sample surface ($\phi_s$), as described by eqn (4):

$$\mathrm{CPD} = \frac{\phi_{\mathrm{tip}} - \phi_{\mathrm{sample}}}{e}. \quad (4)$$

Thus, the observed increase (or decrease) in CPD under positive (or negative) bias corresponds to a decrease (or increase) in the local sample work function, which could be used to quantify the absolute work function of metallic systems,[88] map surface potential distributions in dielectric materials,[89] and identify energy band bending[90] and dopant profiles in semiconductors.[91,92] Additionally, it could be employed to investigate field-induced ionic dynamics, such as the agglomeration of ionic vacancies[93] or proton migration.[94]

In this measurement, external electrical bias was applied locally to the surface of the $VCeO_x$:Ag layer to induce the localized migration of mobile $Ag^+$ species. A metal probe with a sharp metal tip mounted on a micromanipulator stage of the probe station was brought into direct contact with the surface of the $VCeO_x$:Ag layer, and a DC voltage pulse sequence (+5 V or −5 V, 100 times) was applied to induce $Ag^+$ migration within the oxide matrix (Fig. 8a). Subsequently, surface potential mapping was performed *via* KPFM over a 15 × 15 $\mu m^2$ region that encompassed the biased area (Fig. 8b).

Fig. 8c shows the topography of the sample surface after bias application. The dotted regions indicate the location where the probe tip contacted the surface, and line profiles confirm the absence of significant morphological changes. Fig. 8d displays the corresponding surface potential map, clearly revealing distinct contrast between the positive biased and negative biased regions. The line profile in Fig. 8e, which is constructed by the data of Fig. 8d, further quantifies the CPD variations. The region without applied bias, referred to as the initial (pristine) surface, exhibited an average CPD of approximately 140 mV. Upon applying a positive voltage pulse sequence to locally induce a low-resistance state (LRS, *i.e.*, high-conductance state for potentiation), the CPD increased significantly, with the plateau value elevated to approximately 280 mV. In contrast, negative bias results in a comparable decrease in CPD, down to approximately 0 mV, inducing a high-resistance state (HRS, *i.e.*, low-conductance state for depression). Ideally, such modulation would yield a uniform potential shift across the entire biased region; however, in this study, the observed potential distribution showed slight asymmetry and spatial variation. This is likely attributable to the manual probing configuration, which may result in non-uniform contact pressure. Despite these practical limitations, the CPD response exhibited clear polarity-dependent, tunable surface potential, which reflects the work function modulation directly linked to changes in the Fermi level position of the $VCeO_x$:Ag surface. Time-dependent surface potential evolution was monitored to evaluate the stability and reversibility of the induced electronic states. As shown in Fig. 8f, a noticeable decay in CPD was observed over a 94-minute period following positive bias application. This gradual relaxation is indicative of the back-diffusion of $Ag^+$ ions away from the high-density region and supports the hypothesis of reversible ionic motion, in agreement with the previously observed time-dependent synaptic plasticity characteristics. The original 2D and 3D surface potential distributions are provided in Fig. S16.

The mechanism governing the observed surface work function modulation is directly related to the bias-driven redistribution of $Ag^+$ species. As illustrated in Fig. 8g, the application of a positive bias induces the accumulation of mobile Ag ions near the bottom electrode. This accumulation, in turn, facilitates electron injection from the bottom electrode and promotes the filling of surface trap states. Consequently, this leads to an upward shift in the local Fermi level, which effectively lowers the work function and increases the measured CPD. Conversely, a negative bias drives the depletion of Ag ions from the bottom region, which reduces trap occupancy and results in a downward shift in the Fermi level. This process increases the work function and decreases the measured CPD. Collectively, these results provide compelling evidence for the presence of mobile $Ag^+$ species within the $VCeO_x$ matrix. The ability to modulate and

 

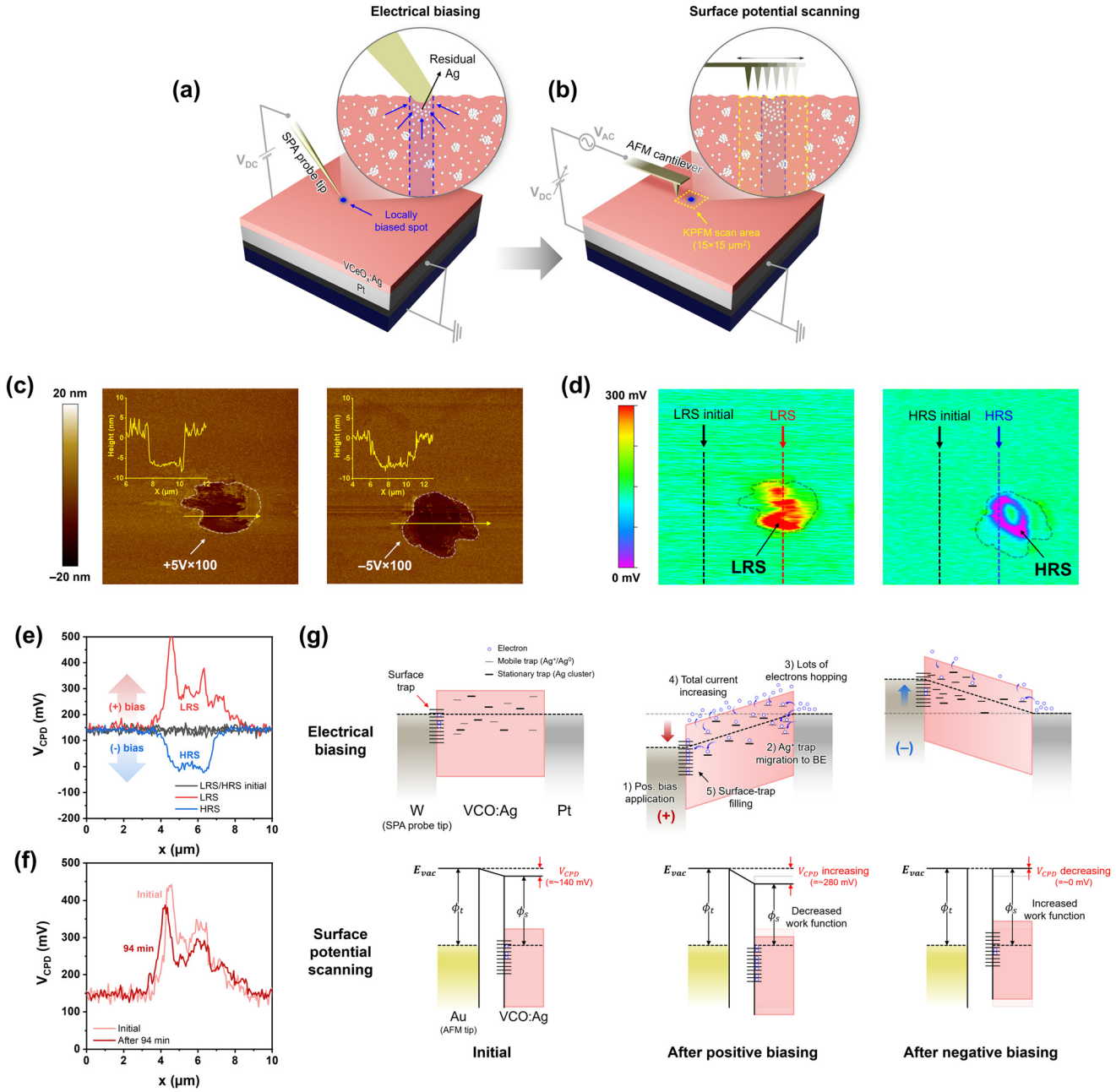


**Fig. 8** (a and b) Schematic of the KPFM experiment on the biased sample. A localized DC bias (+5 V or −5 V, 100 cycles) was applied through a metal probe to induce $Ag^+$ redistribution, followed by static KPFM scanning over a 15 × 15 $\mu m^2$ area. (c) Topography of the biased region. (d) Surface potential map acquired after bias application. (e) Line profile extracted across the biased region revealing clear CPD modulation, with positively biased regions reaching ~280 mV and negatively biased regions dropping to ~0 mV, compared to ~140 mV in the initial state. (f) Time-resolved KPFM profile showing gradual CPD decay after positive bias, indicating reversible ionic migration. (g) Schematic of the bias-dependent trap occupancy and corresponding work function modulation, supporting field-driven redistribution of mobile $Ag^+$ and its role in conductance change.

visualize the change in surface potential by local-bias application as well as the subsequent time-dependent decay, demonstrates that the Ag ions actively migrate under an electric field and partially relax over time. These findings validate the proposed mixed conduction mechanism involving both stationary Ag nanoclusters and mobile ionic $Ag^+$ species, which cooperatively mediate conductance change in this device.

## Conclusions

In this study, the artificial synaptic characteristics of Ag-doped $VCeO_x$ memristor were investigated, revealing its analog conductance-changing behaviors suitable for neuromorphic computing. The proposed devices demonstrated reliable potentiation and depression behavior, robust multilevel con-

ductance modulation, and excellent endurance, enabling precise emulation of biological synaptic plasticity, including time-dependent PPF, PTP, SRDP, and STM-LTM transition. The device's time-dependent synaptic response was further exploited for spatiotemporal data processing *via* RC simulations using experimentally extracted weight update profiles, achieving 4-bit temporal discrimination and classification accuracies of 90.6% and 76.7% for the handwritten digit-MNIST and Fashion-MNIST datasets, respectively. The mechanism for analog conductance modulation was interpreted to involve both mobile $Ag^+$ species and embedded Ag nanoclusters, as confirmed from HR-TEM analysis. The role of mobile Ag ions was further validated by KPFM, which revealed a bias polarity-dependent modulation of the CPD and a time-dependent decay, indicative of reversible ionic migration. These results not only support the proposed trap-mediated, Fermi-level-dependent work function modulation mechanism, but also provide a mechanistic explanation for the observed temporal synaptic plasticity. These synaptic characteristics with temporal dynamics of the Ag-doped $VCeO_x$ memristor offer a promising platform for adaptive, energy-efficient neuromorphic computing systems.

## Author contributions

Jiyeon Ryu: conceptualization, data curation, formal analysis, investigation, visualization, writing – original draft. Peter Hayoung Chung: writing – review & editing. Cheolhwan Yoon: investigation. Minkook Kang: data curation. Hyung-Joon Shin: investigation & Tae-Sik Yoon: funding acquisition, project administration, conceptualization, supervision, writing – review & editing.

## Conflicts of interest

There are no conflicts to declare.

## Data availability

The data supporting this article have been included as part of the supplementary information (SI). The Supplementary Information includes additional figures and experimental data supporting the results discussed in the main text. Supplementary information is available. See DOI: https://doi.org/10.1039/d5nr05056a.

## Acknowledgements

This research was supported by the National Research Foundation (NRF) funded by the Korean Government (MSIT) (No. RS-2024-00401234, No. RS-2024-00406006).

## References

1 M. Jang, H. C. Song, H. J. Kim, J. H. Yoon and K. M. Kim, *Adv. Funct. Mater.*, 2025, **35**, 2423273.
2 M. Kaniselvan, K. Portner, D. F. Falcone, V. Bragaglia, J. Clarysse, L. Begon-Lours, M. Mladenovic, B. J. Offrein and M. Luisier, *ACS Nano*, 2025, **19**, 27455.
3 J. Pyo and S. Kim, *J. Alloys Compd.*, 2022, **896**, 163075.
4 J. Ryu, K. Park, D. P. Sahu and T.-S. Yoon, *ACS Appl. Mater. Interfaces*, 2024, **16**, 26450.
5 K. C. Kwon, J. H. Baek, K. Hong, S. Y. Kim and H. W. Jang, *Nano-Micro Lett.*, 2022, **14**, 58.
6 Y. Lee, Y. Huang, Y. F. Chang, S. J. Yang, N. D. Ignacio, S. Kutagulla, S. Mohan, S. Kim, J. Lee, D. Akinwande and S. Kim, *ACS Nano*, 2024, **18**, 14327.
7 W. Kim, C. Yoo, E. S. Park, M. Ha, J. W. Jeon, G. S. Kim, K. S. Woo, Y. K. Lee and C. S. Hwang, *ACS Appl. Mater. Interfaces*, 2019, **11**, 38910.
8 Z. H. Wu, Y. X. Feng, Y. Liu, H. L. Shi, S. Zhang, Z. K. Liu and Z. Y. Hu, *ACS Appl. Electron. Mater.*, 2021, **3**, 2766.
9 C. Zhuge, J. Jiang, L. Chen, Z. Xie, G. Shen, Y. Fu, Q. Wang and D. He, *ACS Appl. Mater. Interfaces*, 2025, **17**, 34129.
10 R. Li, H. Yang, Y. Zhang, N. Tang, R. Chen, Z. Zhou, L. Liu, J. Kang and P. Huang, *Nanotechnology*, 2023, **34**, 505207.
11 J. Kang, T. Kim, S. Hu, J. Kim, J. Y. Kwak, J. Park, J. K. Park, I. Kim, S. Lee, S. Kim and Y. Jeong, *Nat. Commun.*, 2022, **13**, 4040.
12 S. Choi, S. H. Tan, Z. Li, Y. Kim, C. Choi, P. Y. Chen, H. Yeon, S. Yu and J. Kim, *Nat. Mater.*, 2018, **17**, 335.
13 B. Cho, S. Song, Y. Ji, T. W. Kim and T. Lee, *Adv. Funct. Mater.*, 2011, **21**, 2806.
14 L. Zhou, J. Y. Mao, Y. Ren, J. Q. Yang, S. R. Zhang, Y. Zhou, Q. Liao, Y. J. Zeng, H. Shan, Z. Xu, J. Fu, Y. Wang, X. Chen, Z. Lv, S. T. Han and V. A. L. Roy, *Small*, 2018, **14**, 1800288.
15 J. Park, A. Kumar, Y. Zhou, S. Oh, J. H. Kim, Y. Shi, S. Jain, G. Hota, E. Qiu, A. L. Nagle, I. K. Schuller, C. D. Schuman, G. Cauwenberghs and D. Kuzum, *Nat. Commun.*, 2024, **15**, 3492.
16 P. H. Chung, J. Ryu, D. Seo, D. P. Sahu, M. Song, J. Kim and T. S. Yoon, *Adv. Electron. Mater.*, 2024, **11**, 2400347.
17 K. Park, P. H. Chung, D. P. Sahu and T.-S. Yoon, *Mater. Sci. Semicond. Process.*, 2022, **147**, 106718.
18 J. H. Cha, S. Y. Yang, J. Oh, S. Choi, S. Park, B. C. Jang, W. Ahn and S. Y. Choi, *Nanoscale*, 2020, **12**, 14339.
19 H. C. Cao and H. Ren, *Appl. Phys. Lett.*, 2022, **120**, 133502.
20 Y. Yang, P. Gao, L. Li, X. Pan, S. Tappertzhofen, S. Choi, R. Waser, I. Valov and W. D. Lu, *Nat. Commun.*, 2014, **5**, 4232.
21 S. A. Chekol, S. Menzel, R. W. Ahmad, R. Waser and S. Hoffmann-Eifert, *Adv. Funct. Mater.*, 2021, **32**, 2111242.
22 M. Hellenbrand, B. Bakhit, H. Dou, M. Xiao, M. O. Hill, Z. Sun, A. Mehonic, A. Chen, Q. Jia, H. Wang and J. L. MacManus-Driscoll, *Sci. Adv.*, 2023, **9**, eadg1946.
23 U. Jung, M. Kim, J. Jang, J.-H. Bae, I. M. Kang and S.-H. Lee, *Adv. Sci.*, 2024, **11**, 2307494.

24 A. D. Trofimov, A. V. Emelyanov, A. N. Matsukatova, A. A. Nesmelov, S. A. Zavyalov, T. D. Patsaev, P. A. Forsh, G. Liu, V. V. Rylkov and V. A. Demin, *Nanoscale*, 2025, **17**, 9458.
25 W. Lee, S. Iqbal, J. Kim, S. Lee, J. Lee, M. Kumar and H. Seo, *Appl. Surf. Sci.*, 2023, **639**, 158240.
26 K. H. Chen, C. M. Cheng, M. C. Kao, K. C. Chang, T. C. Chang, T. M. Tsai, S. Wu and F. Y. Su, *J. Electron. Mater.*, 2017, **46**, 2147.
27 W. Wang, B. Zhang and H. Zhao, *Results Phys.*, 2020, **16**, 103001.
28 H. Li, T. Liu, Y. Wang, S. Geng, T. Xu, M. Cao, S. Fan, T. Liu and J. Su, *Ceram. Int.*, 2022, **48**, 13754.
29 H. Zheng, H. J. Kim, P. Yang, J.-S. Park, D. W. Kim, H. H. Lee, C. J. Kang and T.-S. Yoon, *Semicond. Sci. Technol.*, 2017, **32**, 055006.
30 D. P. Sahu, K. Park, J. Han and T.-S. Yoon, *APL Mater.*, 2022, **10**, 051111.
31 S. Guo, H. Arwin, S. Jacobsen, K. Järrendahl and U. Helmersson, *J. Appl. Phys.*, 1995, **77**, 5369.
32 Z. Hu, H. Dou, Y. Zhang, J. Shen, L. Ahmad, S. Han, E. G. Hollander, J. Lu, Y. Zhang, Z. Shang, Y. Cao, J. Huang and H. Wang, *ACS Appl. Mater. Interfaces*, 2024, **16**, 64951.
33 A. Hayat, M. Ratzke, C. A. Chavarin, M. H. Zoellner, A. A. Corley-Wiciak, M. A. Schubert, C. Wenger and I. A. Fischer, *Thin Solid Films*, 2024, **807**, 140547.
34 P.-C. Chen and X. A. Wang, *Mater. Sci. Appl.*, 2020, **11**, 305.
35 J. Shang, W. Xue, Z. Ji, G. Liu, X. Niu, X. Yi, L. Pan, Q. Zhan, X. H. Xu and R. W. Li, *Nanoscale*, 2017, **9**, 7037.
36 N. Raghavan, M. Bosman, D. D. Frey and K. L. Pey, *Microelectron. Reliab.*, 2014, **54**, 2266.
37 D.-T. Wang, Y.-W. Dai, J. Xu, L. Chen, Q.-Q. Sun, P. Zhou, P.-F. Wang, S.-J. Ding and D. W. Zhang, *IEEE Electron Device Lett.*, 2016, **37**, 878.
38 H. Yeon, P. Lin, C. Choi, S. H. Tan, Y. Park, D. Lee, J. Lee, F. Xu, B. Gao, H. Wu, H. Qian, Y. Nie, S. Kim and J. Kim, *Nat. Nanotechnol.*, 2024, **15**, 574–579.
39 D. Ielmini and G. Pedretti, *Chem. Rev.*, 2025, **125**, 5584.
40 N. Dihingia, A. Sadashiva, D. Bhowmik and S. Mondal. 2024 *Device Research Conference (DRC)*.
41 C. Mahata, G. Kim, H. So, M. Ismail, C. C. Hsu, S. Kim and S. Kim, *Adv. Funct. Mater.*, 2024, **35**, 2416862.
42 S. H. Kang, J. Z. Shi, J. Feng, J. M. Fan, S. Xue, G. R. Cai and J. S. Zhao, *ACS Appl. Nano Mater.*, 2023, **6**, 3919.
43 K. J. Lee, Y. C. Weng, L. W. Wang, H. N. Lin, P. Pal, S. Y. Chu, D. Lu and Y. H. Wang, *Nanomaterials*, 2022, **12**, 3252.
44 M. K. Rahmani, M. Ismail, C. Mahata and S. Kim, *Results Phys.*, 2020, **18**, 103325.
45 S. Chandrasekaran, F. M. Simanjuntak, R. Saminathan, D. Panda and T. Y. Tseng, *Nanotechnology*, 2019, **30**, 445205.
46 P. Fang, Q. Wang, T. Lei, Y. Wang, B. Wang, Y. Luo, H. Wu, W. Lv and Z. Zeng, *Appl. Phys. Lett.*, 2023, **122**, 223101.
47 Z. Su, H. Cheng, X. Sun, H. Sun and C. Zuo, *IEEE Electron Device Lett.*, 2023, **44**, 1084.
48 C. He, J. Tang, D. S. Shang, J. Tang, Y. Xi, S. Wang, N. Li, Q. Zhang, J. K. Lu, Z. Wei, Q. Wang, C. Shen, J. Li, S. Shen, J. Shen, R. Yang, D. Shi, H. Wu, S. Wang and G. Zhang, *ACS Appl. Mater. Interfaces*, 2020, **12**, 11945.
49 M. Kim, K. Yoo, S. P. Jeon, S. K. Park and Y. H. Kim, *Micromachines*, 2020, **11**, 154.
50 C. L. Hsu, A. Saleem, A. Singh, D. Kumar and T. Y. Tseng, *IEEE Trans. Electron Devices*, 2021, **68**, 5578.
51 D. Kumar, S. Shrivastava, A. Saleem, A. Singh, H. Lee, Y. H. Wang and T. Y. Tseng, *ACS Appl. Electron. Mater.*, 2022, **4**, 2180.
52 M. U. Khan, C. M. Furqan, J. Kim, S. A. Khan, Q. M. Saqib, M. Y. Chougale, R. A. Shaukat, M. H. Kang, N. P. Kobayashi, J. Bae and H. S. Kwok, *ACS Appl. Electron. Mater.*, 2022, **4**, 297.
53 D. Kim, J. Lee, J. Kim and H. Sohn, *Materials*, 2023, **16**, 4992.
54 D. P. Sahu, K. Park, P. H. Chung, J. M. Han and T. S. Yoon, *Sci. Rep.*, 2023, **13**, 9592.
55 S. Kunwar, Z. Jernigan, Z. Hughes, C. Somodi, M. D. Saccone, F. Caravelli, P. Roy, D. Zhang, H. Y. Wang, Q. X. Jia, J. L. MacManus-Driscoll, G. Kenyon, A. Sornborger, W. Y. Nie and A. P. Chen, *Adv. Intell. Syst.*, 2023, **5**, 2300235.
56 H. J. Zhang, B. Y. Jiang, C. T. Cheng, B. J. Huang, H. Zhang, R. Chen, J. Y. Xu, Y. L. Huang, H. D. Chen, W. H. Pei, Y. Chai and F. C. Zhou, *Nano Lett.*, 2023, **23**, 3107.
57 P. Jetty, U. M. Kannan and S. N. Jammalamadaka, *Nanotechnology*, 2024, **35**, 075701.
58 C. C. Hsu, S. Shrivastava, S. Pratik, S. Chandrasekaran and T. Y. Tseng, *IEEE Trans. Electron Devices*, 2023, **70**, 1048.
59 J. Pan, H. Kan, Z. Liu, S. Gao, E. Wu, Y. Li and C. Zhang, *npj Flexible Electron.*, 2024, **8**, 70.
60 D. Panda, Y. F. Hui and T. Y. Tseng, *Nanoscale*, 2024, **16**, 16148.
61 J. T. Huang, A. Saleem, Y. H. Poh and T. Y. Tseng, *IEEE Trans. Electron Devices*, 2024, **71**, 536.
62 R. M. Shiffrin and R. C. Atkinson, *Psychol. Rev.*, 1969, **76**, 179.
63 A. Laborieux, M. Ernoult, T. Hirtzlin and D. Querlioz, *Nat. Commun.*, 2021, **12**, 2549.
64 W. Zhu and J. Li, *IEEE Access*, 2019, **7**, 163358.
65 X. B. Yin, R. Yang, K. H. Xue, Z. H. Tan, X. D. Zhang, X. S. Miao and X. Guo, *Phys. Chem. Chem. Phys.*, 2016, **18**, 31796.
66 H. Ebbinghaus, *Memory: A Contribution to Experimental Psychology*, 1885.
67 S. G. Hu, Y. Liu, T. P. Chen, Z. Liu, Q. Yu, L. J. Deng, Y. Yin and S. Hosaka, *Appl. Phys. Lett.*, 2013, **103**, 133701.
68 W. Wang, S. Gao, Y. Li, W. Yue, H. Kan, C. Zhang, Z. Lou, L. Wang and G. Shen, *Adv. Funct. Mater.*, 2021, **31**, 2101201.
69 C. S. Yang, D. S. Shang, N. Liu, G. Shi, X. Shen, R. C. Yu, Y. Q. Li and Y. Sun, *Adv. Mater.*, 2017, **29**, 1700906.
70 P. Feng, W. W. Xu, Y. Yang, X. Wan, Y. Shi, Q. Wan, J. W. Zhao and Z. Cui, *Adv. Funct. Mater.*, 2017, **27**, 1604447.

71 Y. N. Zhong, T. Wang, X. Gao, J. L. Xu and S. D. Wang, *Adv. Funct. Mater.*, 2018, **28**, 1800854.
72 Y. Choi, S. Oh, C. Qian, J. H. Park and J. H. Cho, *Nat. Commun.*, 2020, **11**, 4595.
73 G. Liu, C. Wang, W. B. Zhang, L. Pan, C. C. Zhang, X. Yang, F. Fan, Y. Chen and R. W. Li, *Adv. Electron. Mater.*, 2016, **2**, 1500298.
74 S. R. Zhang, L. Zhou, J. Y. Mao, Y. Ren, J. Q. Yang, G. H. Yang, X. Zhu, S. T. Han, V. A. L. Roy and Y. Zhou, *Adv. Mater. Technol.*, 2018, **4**, 1800342.
75 G. Voglis and N. Tavernarakis, *EMBO Rep.*, 2006, **7**, 1104.
76 Y. H. Liu, L. Q. Zhu, P. Feng, Y. Shi and Q. Wan, *Adv. Mater.*, 2015, **27**, 5599.
77 R. S. Zucker and W. G. Regehr, *Annu. Rev. Physiol.*, 2002, **64**, 355.
78 J. D. Lee, B. C. Shim, H. S. Uh and B. G. Park, *IEEE Electron Device Lett.*, 1999, **20**, 215.
79 T. W. Huang, H. Y. Lee, Y. W. Hsieh and C. H. Lee, *J. Cryst. Growth*, 2002, **237**, 492.
80 W. S. Lau, J. Zhang, X. Wan, J. K. Luo, Y. Xu and H. Wong, *AIP Adv.*, 2014, **4**, 027120.
81 S. Yang, T. Kim, S. Kim, D. Chung, T. H. Kim, J. K. Lee, S. Kim, M. Ismail, C. Mahata, S. Kim and S. Cho, *Nanoscale*, 2023, **15**, 14267.
82 S. Roy, G. Niu, Q. Wang, Y. Wang, Y. Zhang, H. Wu, S. Zhai, P. Shi, S. Song, Z. Song, Z. G. Ye, C. Wenger, T. Schroeder, Y. H. Xie, X. Meng, W. Luo and W. Ren, *ACS Appl. Mater. Interfaces*, 2020, **12**, 10648.
83 F. Ma, Z. Xu, Y. Liu, Y. Zheng, W. Chen, H. Hu, T. Guo, F. Li, C. Wu and T. W. Kim, *IEEE Electron Device Lett.*, 2019, **40**, 1610.
84 M. P. McGarry, S. J. Gilbert, L. Yates, M. L. Meyerson, P. G. Kotula, W. B. Bachman, P. A. Sharma, J. D. Flicker, M. P. Siegal and L. B. Biedermann, *J. Appl. Phys.*, 2024, **136**, 055101.
85 C. Grimaldi, *Phys. Rev. B:Condens. Matter Mater. Phys.*, 2014, **89**, 214201.
86 B. Abeles, H. L. Pinch and J. I. Gittleman, *Phys. Rev. Lett.*, 1975, **35**, 247.
87 I. P. Zvyagin and R. Keiper, *Philos. Mag. B*, 2001, **81**, 997.
88 W. Melitz, J. Shen, A. C. Kummel and S. Lee, *Surf. Sci. Rep.*, 2011, **66**, 1.
89 T. Meoded, R. Shikler, N. Fried and Y. Rosenwaks, *Appl. Phys. Lett.*, 1999, **75**, 2435.
90 R. Berger, H. J. Butt, M. B. Retschke and S. A. Weber, *Macromol. Rapid Commun.*, 2009, **30**, 1167.
91 C. Baumgart, M. Helm and H. Schmidt, *Phys. Rev. B: Condens. Matter Mater. Phys.*, 2009, **80**, 085305.
92 J. Liu, J. Jin, Z. Yang, J. Cai, J. Yue, J. Impundu, H. Liu, H. Wei, Z. Peng, Y. J. Li and L. Sun, *ACS Appl. Mater. Interfaces*, 2020, **12**, 31776.
93 D. Li, B. Wu, X. Zhu, J. Wang, B. Ryu, W. D. Lu, W. Lu and X. Liang, *ACS Nano*, 2018, **12**, 9240.
94 T. Dey, X. Lai, S. Manna, K. Patel, R. K. Patel, R. S. Bisht, Y. Zhou, S. Shah, E. Y. Andrei, S. Sankaranarayanan, D. Kuzum, C. Schuman and S. Ramanathan, *ACS Nano*, 2025, **19**, 6815.